Experimental Demonstration of Datagram Switching With Monitoring in Quantum Wrapper Networks

Mehmet Berkay On, Roberto Proietti, Gamze Gül, *Graduate Student Member, IEEE*, Gregory S. Kanter, Sandeep Kumar Singh, Prem Kumar, *Life Fellow, IEEE*, and S. J. Ben Yoo, *Fellow, IEEE*

Abstract—**Adapting the architecture and protocols of classical networks to quantum networking is challenging due to the quantum mechanical properties. In this article, we utilize a Quantum Wrapper Networking architecture that enables transparent and interoperable transportation of quantum wrapper (QW) datagrams, consisting of quantum payloads and classical headers, over optical fiber networks. We experimentally demonstrate end-to-end transportation of QW datagrams in a three-node packet-switched optical network testbed. The header and payload of a QW datagram are multiplexed in time and wavelength, i.e., the 1561.41 nm header precedes the L-band payload. A QW switch/router performs packet switching by reading the headers, generating new headers, and routing the datagrams to their destinations without disturbing quantum information in the payload. We use 20 km fiber links from the source to two distinct destinations in the testbed. Our experiments show >22 coincidence-to-accidental ratio (CAR) for both destinations at two different wavelength channels and clear visibility, $>79\%$. We further investigate impairments such as chromatic dispersion and wavelength-dependent polarization rotations in the fiber. We observe that the classical headers' bit-error rate (BER) and the quantum payloads' CAR are correlated under the wavelength-independent channel attenuation. Thus, QW network control and management can utilize a type of performance monitoring. We also discuss the QW datagram design constraints and future fast packet switching implementations.**

Index Terms—**Quantum networks, quantum communication, packet switching, quantum-classical coexistence.**

I. Introduction

QUANTUM technologies hold the potential to fundamentally transform the way we handle problems in various fields such as metrology [1], telescopy [2], cryptography [3], chemistry [4], communication [5], and computing [6]. While quantum sensors, computers, and key distributors are candidates to solve real-life problems beyond what their classical counterparts are capable of, one evident question is how all these quantum devices are going to interconnect and cooperate. Here, the concept of Quantum Networking emerges. Quantum networks can enable distributed sensing [7] and computing [8] which brings the potential of quantum technologies beyond the single quantum computer and sensor. Although superconducting circuits [9], [10], trapped ions [11], nitrogen-vacancy's electron spin [12] and neutral atoms [13] are candidates that successfully enable quantum processors and memories, photons are the most viable means of actually transporting quantum information over long distances. Today, low-loss transmission of photons over silica fibers provides worldwide classical networks. Thus, we envision that fiber optic will also be enabling infrastructure for quantum networks [14]. However, due to the unique nature of the qubits as quantum information carriers, both hardware components and software stacks of the quantum networks should be carefully designed. For example, the no-cloning theorem dictates that an arbitrary unknown quantum state of a photon can not be copied [15]. Therefore, regenerating or amplifying qubits is not possible in quantum networks and in most applications, performance monitoring by power tapping qubits at the intermediate nodes of the networks is not an option. Thus, quantum networks require divergent approaches than classical networks to guarantee network integrity with some level of quality of transmission.

Switching and routing of packets in quantum networks that need to accommodate multiple applications present another challenge. Classical data payloads and packet labels are the same in nature; both are represented by multiple photons in the fibers. The classical routers can detect the packets and handle the forwarding in the electrical domain. However, the quantum data payloads have divergent characteristics compared to the packet labels. Quantum Network Routers should be aware of the nature of quantum network packets and handle the payloads and labels separately in the physical layer. There have been multiple successfully demonstrated multi-node quantum networks for quantum key distribution (QKD) [16], [17], [18], [19] and entanglement distribution applications [20], [21], [22]. Moreover, Dahlberg et al. [23] proposed a link layer protocol for the quantum networks; Alia et al. [24] demonstrated dynamic reconfiguration in software-defined quantum networks,

---

Manuscript received 18 October 2023; revised 23 December 2023; accepted 1 February 2024. Date of publication 5 February 2024; date of current version 16 May 2024. This work was supported in part by the U.S. DOE ASCR Program under Award DE-SC-0022336, in part by NSF ICE-T:RC under Award 1836921, and in part by European Union's Horizon Europe Research and Innovation Programme under Grant 101092766 (ALLEGRO Project). *(Corresponding author: S. J. Ben Yoo.)*

Mehmet Berkay On and S. J. Ben Yoo are with the Department of Electrical and Computer Engineering, University of California, Davis, CA 95616 USA (e-mail: sbyoo@ucdavis.edu).

Roberto Proietti is with the Department of Electronics and Telecommunications Engineering, Politecnico di Torino, 10129 Torino, Italy.

Gamze Gül, Gregory S. Kanter, and Prem Kumar are with the Center for Photonic Communication and Computing, Department of Electrical and Computer Engineering, Northwestern University, Evanston, IL 60208 USA (e-mail: kumarp@northwestern.edu).

Sandeep Kumar Singh is with the Department of Electronics and Communication Engineering, Indian Institute of Technology, Roorkee 247667, India.

Color versions of one or more figures in this article are available at https://doi.org/10.1109/JLT.2024.3362292.

Digital Object Identifier 10.1109/JLT.2024.3362292

and Lee et al. [25] architected a quantum router for entanglement traffic. However, to the best of our knowledge, switching the quantum packets and monitoring the quality of transmission while considering the distinctive nature of the headers and the payloads in the physical layer have yet to be addressed. Although Lucio-Martinez et al. [26] experimentally demonstrated classical frame bits precede the QKD data frames in the point-to-point link, switching the quantum data frames has not been discussed. Similarly, DiAdamo et al. [27] introduced the packet-switched quantum networks conceptually; however, the proposed architecture has not been realized on an experimental testbed.

To address the issues mentioned above, Yoo and Kumar [28] proposed the Quantum Wrapper Networking (QWN) architecture, inspired by optical packet switching for classical internet [29]. The QWN relies on the quantum wrapper (QW) datagram, which consists of classical label bits and quantum data payloads. QWNs promise low latency transmission, high channel utilization, and robust signaling for future quantum networks. The QWN architecture and capabilities are discussed in detail [30], and the coexistence of the classical label bits with the quantum data bits is investigated in [31]. Further, we presented that we can infer information about the quality of the quantum channel from the classical label bit-error rate in point-to-point QWN links [32].

In this article, we demonstrate quantum datagram switching in a three-node Quantum Wrapper Network. A source node generates QWN packets with classical label bits and quantum data payloads. A QW switch reads the classical labels and forwards the quantum payload (without disturbing it) to one of the two distinct destinations in our testbed. We measure coincidence counts after transmission over 20 km of optical fiber with >22 coincidence-to-accidental-count ratio (CAR) for both destinations, and investigate impairments such as chromatic dispersion and polarization rotations for >30 nm broadband quantum signals. We also perform two-photon interference measurements of $>79\%$ visibility at both destinations and with two polarization bases. Further, we observe the linear correlation between the quality of classical label bits and the quality of quantum data payloads for three separate paths in our testbed. The reported results can lead to performance monitoring and route optimization in future QWNs. Lastly, we analyze the QWN design constraints, such as packet switching time and label content. Our current implementation uses a relatively long clock and data recovery pilot sequence of $>40\ \mu$s duration, but we discuss means to reduce this overhead to enable compatibility with nanosecond-range packet switching times.

II. QUANTUM WRAPPER NETWORKING ARCHITECTURE

'Quantum Wrapper' is a new quantum networking technology that enables end-to-end transportation of quantum data payloads without altering their states in the intermediate network nodes. The quantum payloads can be in an arbitrary format like discrete-variable, continuous-variable, time-bin, polarization-entangled, etc. The classical headers and, optionally tail bits, wrap the payloads and contain network control and management information such as routing, multiplexing, timing, formatting, etc. Fig. 1 presents one example of the header content. When the quantum payloads can be variable in size depending on the application, QW allows MPLS (Multi-Protocol Label Switching)-like switching and traffic engineering. The QW can coexist with classical data communication channels by wavelength division multiplexing (WDM) and supports control and management plane communications for software-defined networks (SDN). QWN does not require global synchronization thanks to the classical headers, which can synchronize the network nodes and deliver timing information. QW Switch/Routers (QWSR) are interface devices that employ quantum-aware optical frontend and QW network interface card (QWNIC) electronics.

A. QWSR At the Edge

The main functionalities of the QWSRs at the edge are to form, transmit, and receive the QW datagrams. A QWNIC is equipped with optical transceivers to generate and analyze the headers. Additionally, it communicates with the quantum local area network (QLAN) clients. Either individual QLAN clients can generate the quantum payloads or request from QWSR. QWSR can employ quantum sources such as attenuated coherent light-based or entangled photon pair-based sources. Moreover, a transducer [33], [34], [35] should be employed at the QWSR and convert superconducting qubits to telecom wavelength qubits to be transmitted to remote nodes. Therefore, QLAN clients do not have to be photonics-based quantum devices. Similarly, QWSR can employ single photon detectors and optical equipment like beam splitters, polarization controllers and photonic-based simple quantum gates to perform quantum measurements for the clients, or the QWSR can deliver quantum payloads to local quantum receivers without disturbing the qubits. Timing is critical to (un)wrap the datagrams as well as quantum state measurements. Therefore, QWNIC should synchronize with any local quantum transceivers. Fig. 1 summarizes the functionalities and the communication links of the QWSR at the edge nodes. Here, the header and payload occupy different wavelength channels; therefore, a passive WDM (de)multiplexer performs (un)wrapping of datagrams. As discussed in [30], the header and payload can utilize the same wavelength channel as well. In such cases, a fast, low-loss, high isolation 1×2 optical switches perform (un)wrapping of the datagrams.

B. QWSR At the Core

QWSR at the core performs packet switching for QW datagrams. By default, QWSR looks for the headers initially. The header contents include the starting time and duration of the payload. QWSR at the core unwraps the payload, delays for a short period, wraps with new classical headers, and routes the new datagrams to their destination. QWNIC communicates with NC&M to access the routing table and configure the optical switching fabric accordingly. Further, QWSR can employ single photon detectors and necessary optical devices for Bell state measurements. Therefore, entanglement between the quantum payloads can be swapped [36], [37], [38]. Entanglement swapping is a crucial quantum feature where the longer transmission distance can be supported [39]. However, it requires stringent

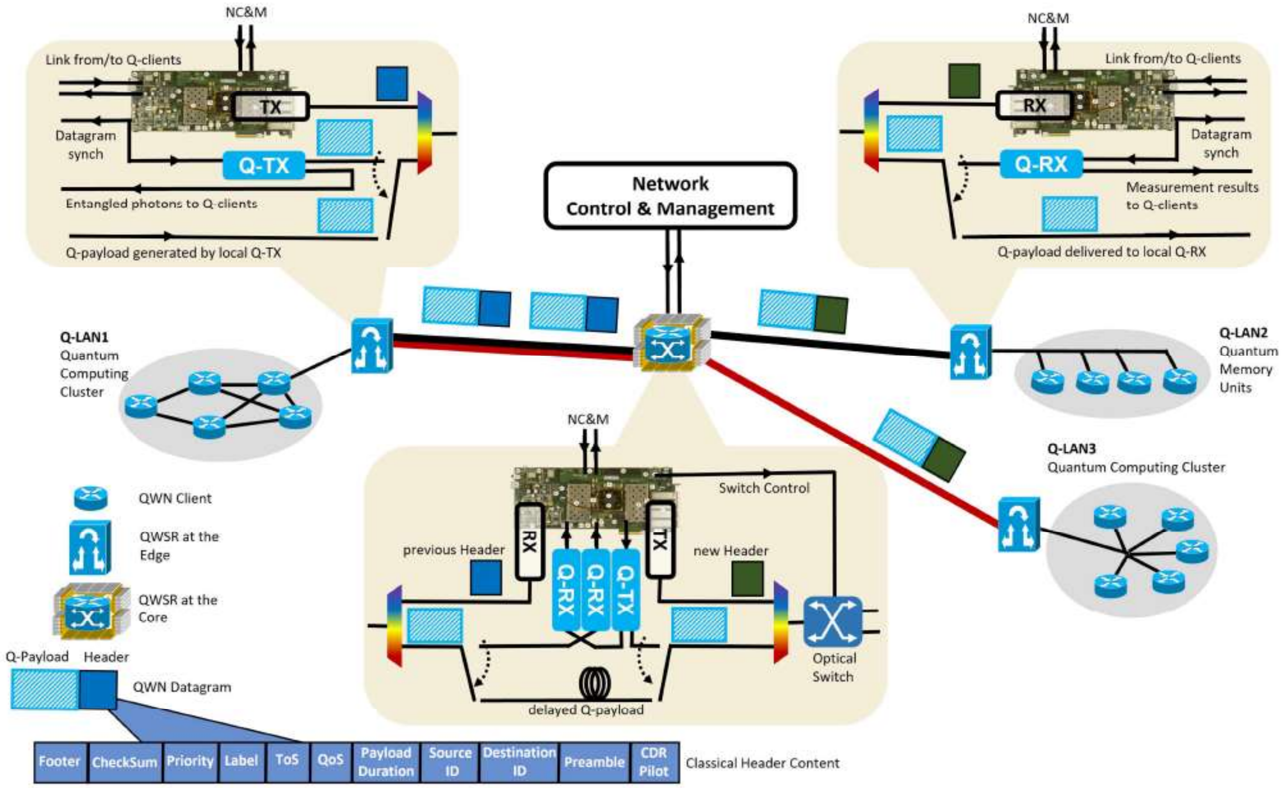

Fig. 1. Conceptual diagram of the experimentally realized three-node QWN. QWSR at the edge which consists of optical front-end components and QWNIC electronics, is presented in detail as a QW datagram transmitter and receiver. QWSRs at the edge are able to serve any type of QLAN clients such as quantum processing units. quantum memories, quantum sensors, quantum key distributors etc. QW datagrams utilize both wavelength and time multiplexing of the quantum payloads and the classical headers. QWSR at the core is also presented in detail, which can forward quantum payloads without measuring, or optionally perform Bell state measurements to support all generations of quantum repeaters. QWSR at the core reads, updates, and regenerates classical header content. NC&M communicates with all QWSRs through a dedicated classical channel.

timing during the joint measurement between arriving photons at QWSR. The classical header can also coordinate the timing between entanglement-swapping parties for heralding. In the future, QWN can support the next generation of quantum repeaters [40]. QWSR equipped with high-fidelity quantum gates can perform quantum error correction at the cores and edges of the network. Briefly, QWN supports any buffering from more straightforward approaches such as fiber delay lines to complex quantum technologies like quantum repeater/memories.

C. Channel Monitoring in QWN

In classical networks, electronics in linecards and network elements at intermediate nodes can easily handle monitoring functions such as signal integrity, bit errors, framing errors, etc. However, a similar approach does not apply to quantum networks due to the nature of the quantum packets. Quantum Wrapper Networks utilize the classical headers to monitor physical layer impairments. Even though qubits and classical bits are fundamentally different, fiber-optic channel impairments such as dispersion, polarization state rotations, and excess loss affect the qubits and classical bits similarly to some extent. To elaborate, the attenuation in the link degrades the received optical power, which results in a lower signal-to-noise ratio and, consequently, higher classical bit-error rates. In the meantime, the attenuation increases the probability of photon loss; therefore, single photon qubit receivers click less frequently, which results in lower visibility and coincidence-to-accidental ratios of the quantum payload. Therefore, QWN linecards at edge nodes and the interface components at intermediate nodes can sense the path losses and infer the quantum channel quality of transmission without touching the quantum data. However, there are design requirements to guarantee accurate monitoring. The fiber-optic channel impairments can be time-varying and wavelength-dependent. If the target impairment is time-varying, such as polarization state rotations, the QW datagram duration should be much shorter than the time it takes for the polarization state to appreciably drift. In other words, the classical header bits and the payload qubits must observe identical polarization rotations. Besides, impairments such as dispersion, attenuation, etc. might be wavelength-dependent. In such cases, the classical headers must be assigned to the same wavelength channel as the quantum payloads or as close as possible so that single-photon qubits and multi-photon classical bits observe similar imprints.

III. EXPERIMENTAL SETUP

In our lab environment, we built an experimental testbed that implements the three-node network conceptually illustrated in

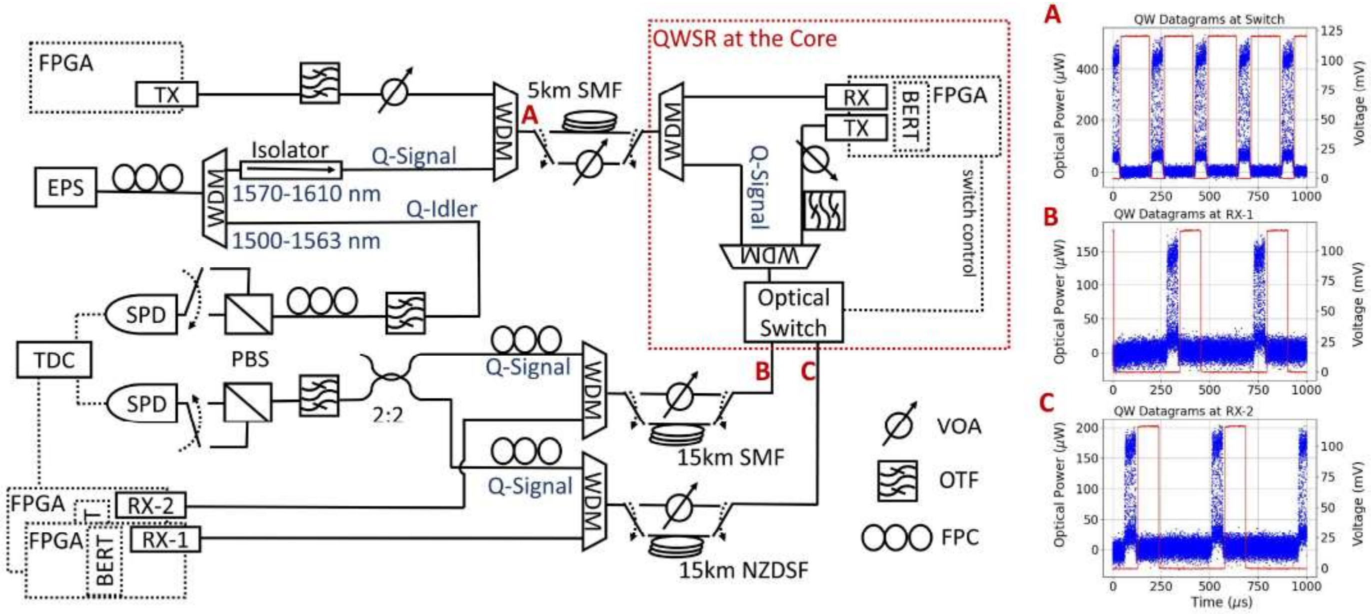

Fig. 2. Detailed experimental setup and QW datagrams under scope at points A, B, and C, marked in red. Blue traces in the plots are optical power levels of the datagram, while red traces are electrical signal outputs from the header receivers, indicating the payload period.

Fig. 1. QWSR at the edge, connected to QLAN1, employs an entangled photon source, measures one of the entangled photons locally, and distributes the other to the QWSR at the destination edges. Entanglement distribution is the enabling feature of the quantum networks for the applications such as long-distance QKD [41], longer-baseline interferometers [2], distributed sensing [7], and computing [8]. Fig. 2 presents the details of the experimental setup and the QW datagrams. A digital communication analyzer (DCA) monitors QW datagrams at points A, B, and C. The source node periodically transmits datagrams while adjacent datagrams are designated to send different destinations. At point A, the datagrams are received by QWSR at the core. A passive wavelength-division demultiplexer (WDM) unwraps the datagrams to the header and the payload. After receiving the destination ID in the header, QWSR starts to transmit new header and reconfigures the optical switch to route new datagrams to its destination. As seen at points B and C, an optical switch switches adjacent datagrams to different fiber paths. The optical switch (NanoSpeed from Agiltron) is polarization and wavelength insensitive, with $<$50 ns switching time. The DCA can not detect quantum payloads due to low power levels. However, QW headers include the payload duration information. Therefore, both QWSR at the core and destinations recognize the beginning and end of the payloads. Red traces in Fig. 2 mark the payload in time which are electrical signals driven by field programmable gate array (FPGA) boards. At the destination nodes, the electrical signals synchronize and trigger the time-to-digital converter (TDC) circuits for coincidence count (CC) measurements. There is a 5 km single mode fiber (SMF-28) spool between the source and QWSR node. After the QWSR, link-1 has 15 km SMF spool while link-2 has 15 km non-zero dispersion shifted fiber (NZDSF) spool. Later, we replace the fiber spools with variable optical attenuators (VOAs) to observe the correlation between the header bit-error-rate (BER) and the payload coincidence-to-accidental ratio (CAR).

A. *Quantum Payload Transceiver*

A periodically-poled silica fiber-based entangled photon source (EPS-1000 from OZ Optics) generates broadband polarization-entangled photons in the quantum state of $|\Psi\rangle = \frac{1}{\sqrt{2}}(|HV\rangle + |VH\rangle)$ by type-II phasematched spontaneous parametric down-conversion process. The EPS is continuously pumped at 782.8 nm and the center of the pair is around 1565.75 nm. A thin film coating-based 3-port WDM demultiplexer (from AC photonics) separates the pair as *signal* at L-band and *idler* at C-band. An isolator prevents *idler* channel from reflected photons by classical components. While *signal* photons are multiplexed with the headers and transmitted through the networking testbed, *idler* photons are directly connected to a reference quantum receiver. Front-end of the quantum receiver consists of an optical tunable filter (OTF) to slice the broadband quantum channel to narrower bands, a fiber-based polarization controller (FPC), and a polarization beam splitter (PBS). A pair of InGaAs avalanche photodiodes (from Aurea Technology) works as single photon detectors (SPD). A mechanical low-speed fiber switch connects SPD to both output ports of PBS. Therefore we can measure CC in four combinations, HH, HV, VH, and VV (H as horizontal and V as vertical polarization). A time-to-digital converter (TDC) circuit digitizes the photons' arrival time and calculates the arrival time difference between the SPDs. The electrical signals (shown in Fig. 2 B and C as red trace) from the header receivers are combined by an "or" gate and connected to the TDC module as an external clock source. Because of the availability of only two SPDs in the lab environment, we use a 50:50 power coupler which combines

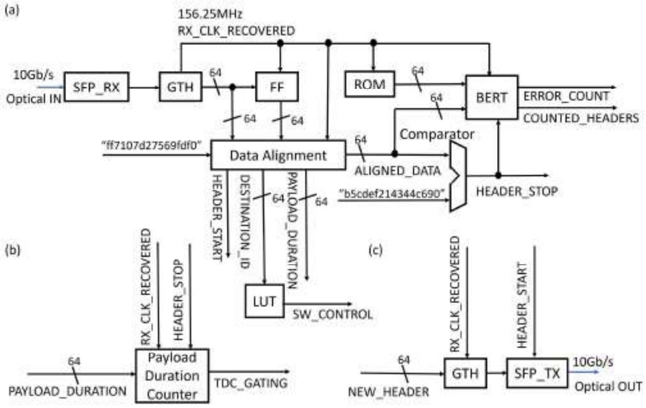

Fig. 3. Digital implementation of the (a) header receiver, (b) payload duration counter circuit, and (c) new header transmitter.

quantum payloads of both destinations after the datagrams are unwrapped. Although both links are around 20 km in length, due to the meters range variation of the spools, we are able to separate CC locations of the destinations in time domain as seen in Figs. 4 and 5.

B. Classical Header Transceiver

Commercial dense WDM small form factor pluggable (SFP) transceivers transmit and receive the headers at 10 Gbps data rate. The classical header occupies ITU grid channel #20, 1561.41 nm. Every node employs a separate Virtex-7 series VC709 FPGA board which drives optical transceivers and external devices such as the optical switch at QWSR node and the TDC at destination nodes. Although a QW header can carry various networking information as seen in Fig. 1, the header in this experiment consists of six parts; clock-data recovery (CDR) pilot, preamble, destination ID, payload duration, footer, and multiple copies of $2^{11}-1$ pseudo-random bit sequence (PRBS). The total header duration of 58.85 μs includes 41.6 μs of CDR pilot sequence, 13.1 μs of PRBS sequence. The preamble, footer, destination ID, and payload duration sequences are 64 bits in length each. The header also includes 4.12 μs laser shut-down period. Through the FPGA logic, we power down the transmitter's (TX) laser during the payload transmission, unlike our previous work [32] where we used an external Mach-Zehnder modulator to create burst-mode headers. The previous implementation suffered from the modulators' limited extinction ratio. Here, there are no classical header photons emitted during the time of the payload. When the TX laser is powered on during the beginning of the CDR pilot sequence, it requires around 6 μs to settle at a constant output power. This time is also considered inside the CDR pilot sequence. On the other hand, the quantum payloads are 149.12 μs. Before and after the payloads, we assigned a total 16 μs guard time. The guard time accounts for the power-down time of TX's laser, response time of the electronics, optical switch, TDC, etc., and the dispersion [42] while the headers and payloads are assigned to different wavelength channels. In the future, the guard time can be designed more precisely to improve throughput. Therefore, the duration of one experimental QW datagram is 223.98 μs.

Note that, there is no fundamental limitation for QW datagram timing design. QW datagrams can be customized depending on the network protocol and application needs. Although we emulate same-length datagrams for simplicity in the experiment, adjacent QW datagrams can also be designed in various lengths. However, one requirement is the CDR pilot sequence length. We investigate the effects of CDR pilot sequence length in depth in Section IV-E. Because the header receiver (RX) at the QWSR node can not identify the header information before the CDR circuit is locked, the payload must be either delayed by fiber delay lines at the QWSR, or truncated. If a fiber delay line is employed, its length should be around 8 km to compensate 41.6 μs CDR pilot length, which is not practical in terms of loss budget of QWNs. Mandil et al. [43] also discussed and simulated similar trade-offs for the packet-switched QKD networks. We truncate payload duration after the QWSR node and propose possible solutions to reduce CDR pilot sequence length to nanosecond levels in Section IV-E.

Fig. 3 illustrates the digital implementation of the header RX and the header regeneration at QWSR. Gigabit Transceiver (GTH) module controls the optical transceivers and utilizes a 64-to-1 serializer/deserializer. Therefore, the recovered clock, RX_CLK_RECOVERED, is at 156.25 MHz, which synchronizes external modules with the incoming data stream. First, by looking at the header preamble (*"ff7107d27569fdf0"* in hexadecimal), the data is aligned. HEADER_START bit indicates the detected preamble. Following 64-bit sequences after the preamble are DESTINATION_ID and PAYLOAD_DURATION. A look-up table (LUT) selects the switch control bit according to DESTINATION_ID. ALIGNED_DATA stream is fed to the BER tester (BERT), which returns the number of counted headers and total error counts. A comparator looks for the footer (*"b5cdef214344c690"* in hexadecimal) in the ALIGNED_DATA, indicating the end of the header. As seen in Fig. 3(b), PAYLOAD_DURATION is fed to the payload duration counter, which generates external output for gating TDC (red electrical traces in Fig. 2) right after the HEADER_STOP turns high. The header regenerator TX, shown in Fig. 3(c), immediately powers on the TX's laser and starts to transmit the new header's CDR pilot sequence when the received HEADER_START bit turns high. The new header's destination ID and payload duration are updated accordingly. As explained earlier, the new payload duration is reduced in the new header. The rest of the header contents stays unchanged.

IV. RESULTS AND DISCUSSION

We perform coincidence count measurements in four combinations of the polarization axes, HH, HV, VH, and VV (first letter signifies the *signal* channel axis, and the second *idler* channel axis). During the CC measurements, SPDs operate at 20% quantum efficiency and 100 μs dead time. Multiple payloads are aggregated to gather enough statistics. From the CC values, we calculate coincidence-to-accidental ratio (CAR), $\mathrm{CAR} = (\mathrm{CC}_{\max}/\mathrm{CC}_{\mathrm{accidental}})$ as a quality of quantum channel

(a) with 1nm 3dB BW optical filters at Q-signal 1574.0nm, Q-idler 1557.5nm

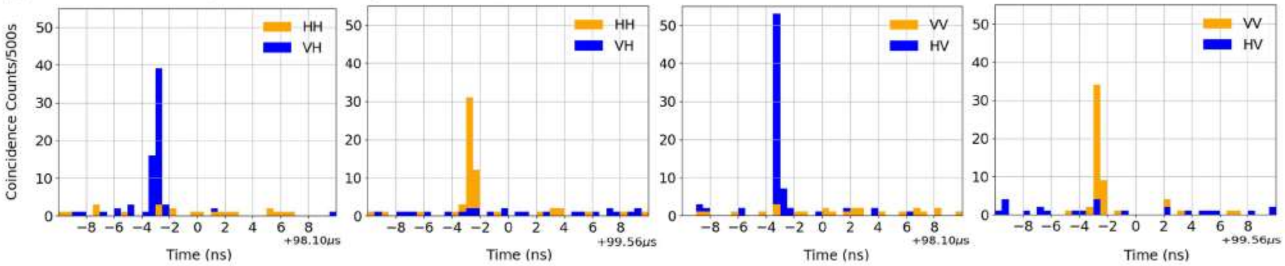

(b) w/o optical filters >30nm BW

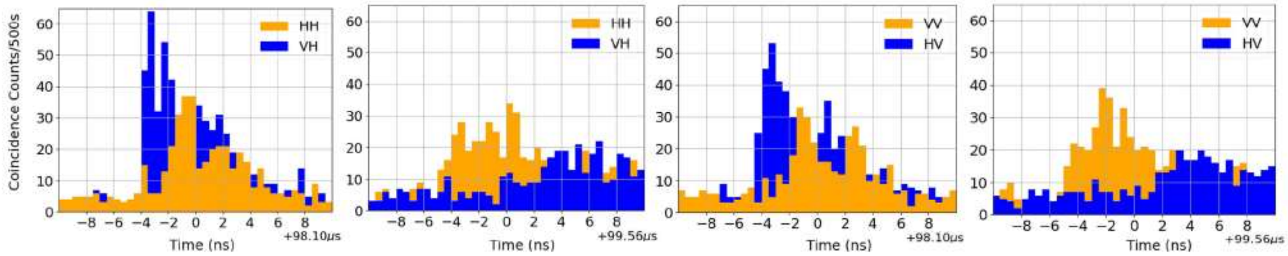

Fig. 4. Coincidence counts distributions, first-row plots with narrow-band photon pairs at (1574.0, 1557.5) nm, second-row plots with broadband photon pairs. The first and third column plots represent destination-2 measurements, around 98.10 μs delay. The second and fourth column plots represent destination-1 measurements, around 99.56 μs delay.

(a) with 1nm 3dB BW optical filters at Q-signal 1584.0nm, Q-idler 1547.5nm

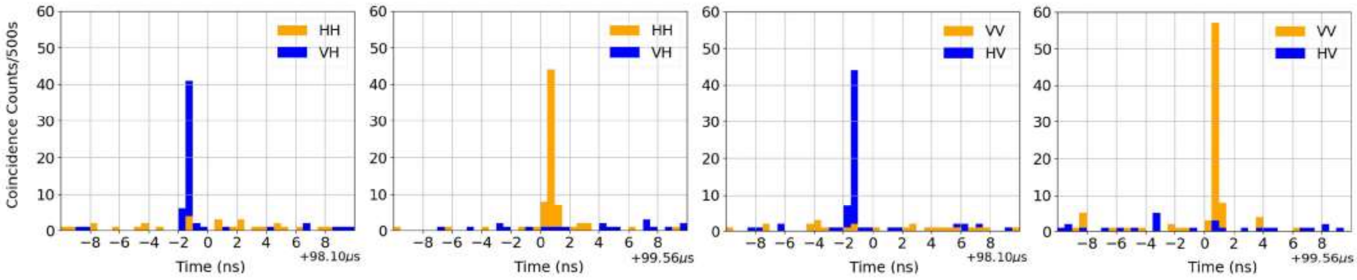

(b) w/o optical filters >30nm BW

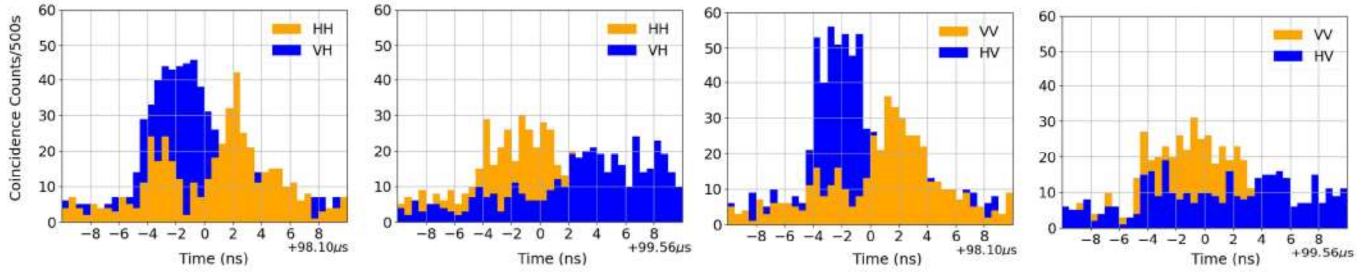

Fig. 5. Coincidence counts distributions, first-row plots with narrow-band photon pairs at (1584.0, 1547.5) nm, second-row plots with broadband photon pairs. The first and third column plots represent destination-2 measurements, around 98.10 μs delay. The second and fourth column plots represent destination-1 measurements, around 99.56 μs delay.

metric [44]. CAR is analogous to classical communication's signal-to-noise ratio (SNR). When the polarization controllers (PC) compensate for the polarization state rotation due to transmission, $\mathrm{CC}_{\max}$ appears at either (HH, VV) or (HV, VH) combinations due to our EPS characteristic. We intentionally aligned different destinations' PCs as orthogonal such that the $\mathrm{CC}_{\max}$ occurs at different polarization combinations. We use a single-polarization classical light source at the same wavelength with the quantum channel for the polarization alignment and achieve >20 dB extinction ratio on PBSs.

A. Fiber Transmission

QW datagrams are transmitted over 5 km SMF from the source node to the QWSR node. After reading the headers and switching packets, destination-1's datagrams travel 15 km SMF path. $\mathrm{CC}_{\max}$ appears around 99.56 μs delay, and (HH, VV) polarization combinations. In the meantime, destination-2's datagrams travel 15 km NZDSF path, and $\mathrm{CC}_{\max}$ appears around 98.10 μs at (HV, VH) polarization combinations. We investigate narrow-band quantum channel transmission by using

1 nm 3 dB bandwidth (BW) OTF at *idler* channel and 5 nm 3 dB BW OTF at *signal* channel. We recorded CC measurements at four polarization combinations for pairs at (1574.0, 1557.5) nm and (1584.0, 1547.5) nm for (*idler*, *signal*) respectively. Figs. 4 and 5(a) represent the CC measurement results.

We observe that moving *signal* channel 10 nm longer wavelength results in destination-2 *signal* photons arriving 2 ns late. On the other hand, destination-1 *signal* photons arrive 4 ns late due to chromatic dispersion in the fiber. CAR values are 25.2 ± 0.7 for destination-1 and 29.1 ± 1.9 for destination-2 at (1574.0, 1557.5) nm. Similarly at (1584.0, 1547.5) nm, CAR values are 30.5 ± 1.9 for destination-1 and 22 ± 1.5 for destination-2. Later, we removed the OTF on both *signal* and *idler* channel; therefore >30 nm quantum channel is transmitted over the fiber link. Figs. 4 and 5(b) plots represent the CC measurement results for the broadband channel. As expected, $\mathrm{CC}_{\mathrm{max}}$ peaks are broadened due to chromatic dispersion. The broadening is more severe at destination-1, while destination-2's datagrams propagate through less dispersive NZDSF. Note that PC alignment is still performed at single wavelength. Therefore, we can observe clear extinction between the orthogonal polarization axes only at the same time slot as the narrow band channel. The extinction ratio degrades at different time slots, which is due to the dispersion corresponding to photons at different wavelengths. For some time slots the VV polarization basis state that corresponds to a CC minimum at the alignment wavelength can even exceed the HV CC rate. We concluded that birefringence in the fiber spools is wavelength-dependent; therefore, a single PC at the quantum RX can not compensate for polarization rotations in the link for broadband channels. CAR values of the broadband channel are 4.8 ± 1.5 (3.5 ± 0.4) in destination-1 and 12 ± 1.5 (10.2 ± 0.4) in destination-2, shown in Fig. 4 (Fig. 5).

B. Wavelength Dependent Polarization Rotation

We further investigate the wavelength-dependent birefringence in the links. Instead of dual polarization output photons from EPS, we polarize the output photons by using a fiber-based inline polarizer. Therefore, only horizontally polarized broadband photons are transmitted. Both destination-1 and destination-2 align their polarization control at 1584 nm. Later, we tune the OTF at *signal* channel and record counts per second from both output ports of PBS. Fig. 6 shows the continuous count rates (not packetized) at the H and V output ports of the PBS. Due to wavelength dependence, the current testbed headers, that are >10 nm shorter than quantum *signal* channel, can not monitor the polarization state rotations in the transmission link. To achieve polarization state monitoring, the QW headers could be assigned to the same wavelength channel or dummy supervisory quantum payloads could be transmitted [30].

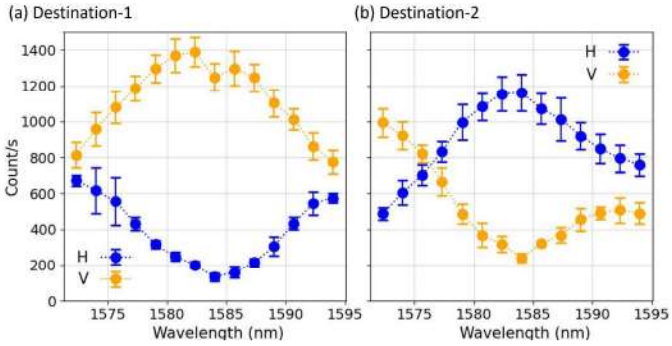

Fig. 6. Count rates for the polarized photons input vs. central wavelength of the OTF at (a) destination-1 and (b) destination-2 receivers.

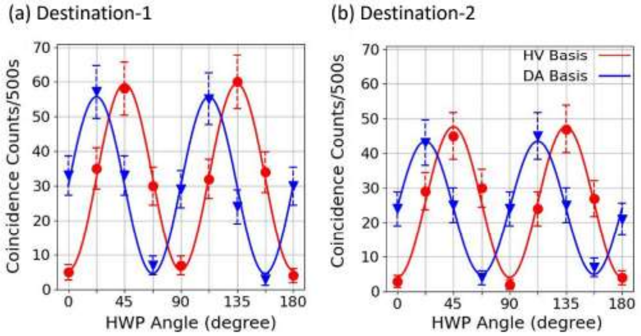

Fig. 7. Coincidence counts per 500 seconds with varying half-wave plate angle at (a) destination-1 and (b) destination-2 quantum receivers.

C. Two-Photon Interference Measurements

The experimental setup in Fig. 2 employs fiber-based polarization beam splitters and controllers. Therefore, only purely horizontal (H) and vertical (V) polarizations can be identified by maximizing the extinction ratio between two ports of PBS. Fiber-to-fiber U-benchs (from Thorlabs), consisting of two collimators and a free-space rotatable linear polarizer, replace PBSs in the Fig. 2. *Idler* channel's U-bench has a half-wave plate (HWP) before the linear polarizer to perform CC measurements of the packet switched quantum payloads on different linear polarization alignments. For each measurement point in Fig. 7, HWP is rotated approximately 22.5°. At the HV basis alignment *signal* channel's linear polarizer is set to 0° while at the DA basis, set to 45°. Fig. 7 summarizes the two-photon interference fringes with sinusoidal fitting, $f(x) = Asin(4(\theta_{HWP} - \theta_0)) + C$ at destination-1 and destination-2 receivers. θ_0 is 22.5° for HV basis and 0° for DA basis, shown as solid lines in Fig. 7. Visibility as a measure of the contrast in the interference fringe is calculated as the ratio A/C. We report 83% (85%) visibility at destination-1 and 84% (79%) at destination-2 for HV (DA) basis alignments.

D. Monitoring Quantum Channel Quality

Classical header bits travel the same link with quantum payloads as a QW datagram. As discussed in Section II, the headers can be helpful to monitor channel impairment. One of these impairments is the path loss in the network. We investigate the correlation between the header BER and quantum channel CAR in the three nodes of the QWN testbed. Kilometers range fiber spools are replaced with VOAs. The QWSR and destination nodes' header RXs can perform BER

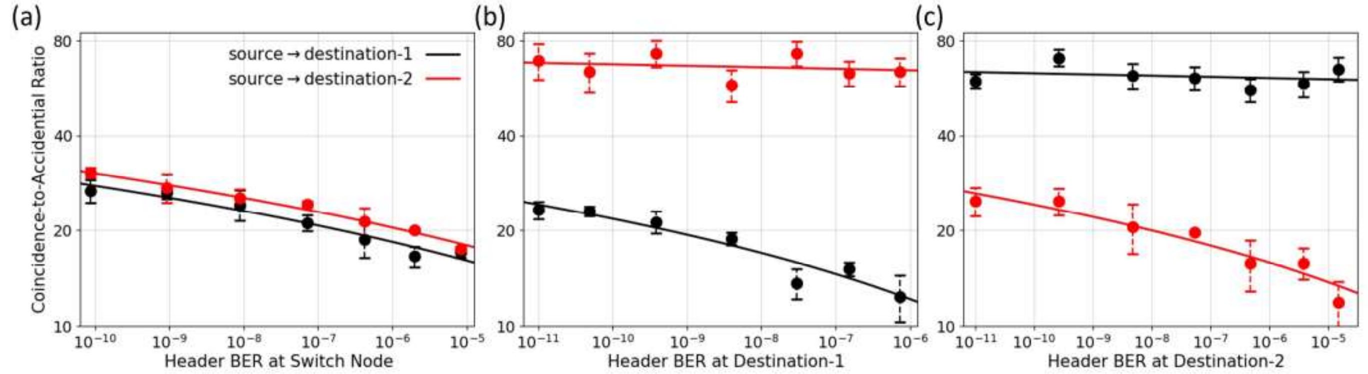

Fig. 8. CAR of the quantum payloads vs. (a) header BER measured at switch node for the path from source to QWSR, (b) header BER measured at destination-1 for the path from QWSR to destination-1, and (c) header BER measured at destination-2 for the path from QWSR to destination-2.

measurements of the classical headers. Therefore, we can monitor three paths in the network: from source to QWSR, from QWSR to destination-1 and from QWSR to destination-2. CAR measurements are performed at the destination nodes' quantum RX. Before introducing the attenuation in the paths, header TXs adjust their launch power to a level where an additional 0.5 dB attenuation introduces noticeable BER degradation. Later, this adjustment between the header transceivers can be achieved by an initialization cycle before transmitting datagrams. Fig. 8 plots show the correlation between the header BER and quantum payload CAR. There is 0.5 dB attenuation difference between adjacent measurement points. It is expected that the extra loss in the link degrades classical channel SNR and, therefore, results in higher header BER. Similarly, the extra loss increases the probability of the *signal* photon loss, resulting in lower CAR. First, the variable attenuation is introduced at the first path, from source to QWSR. Here, datagrams designated to destination-1 and destination-2 travel the path together. Fig. 8(a) presents the correlation between the header BER and quantum CAR for both destinations. Later, variable attenuation is introduced at the second path, from QWSR to destination-1. As seen in Fig. 8(b), the header BER measurements at the destination-1 node correlate with destination-1 quantum channel CAR, while the datagrams from destination-2 do not travel through the second path, CAR is constant. It is vice versa for the third path where only destination-2's datagrams travel through the introduced loss, shown in Fig. 8(c). Note that, for the point-to-point transmission, only the end node receivers that perform the quantum measurement can report the quantum channel quality. However, network controllers can not identify which path in the link has excess propagation loss. In the QWN, QWSR nodes at the core and the edge can inform the NC&M about the header BER. In this way, NC&M can monitor every path individually in the network without performing quantum measurement, and further, it can optimize the routing for the maximum estimated quantum channel quality.

E. Burst-Mode Header Performance

The design of the header in QWN can be flexible and support multiple packet formats simultaneously. However, the CDR pilot is a necessary sequence in the header. When the QWSR header RX starts to receive the header bits, it needs to recover the clock and align the data so that header content can be identified correctly. The required time for the CDR depends on the receiver characteristic and received optical power [45]. The experimentally realized headers utilize 41.6 μs long CDR pilot sequence. We perform BERT in the QWSR at the core (blue trace in Fig. 9) and the edge (green and orange traces in Fig. 9)

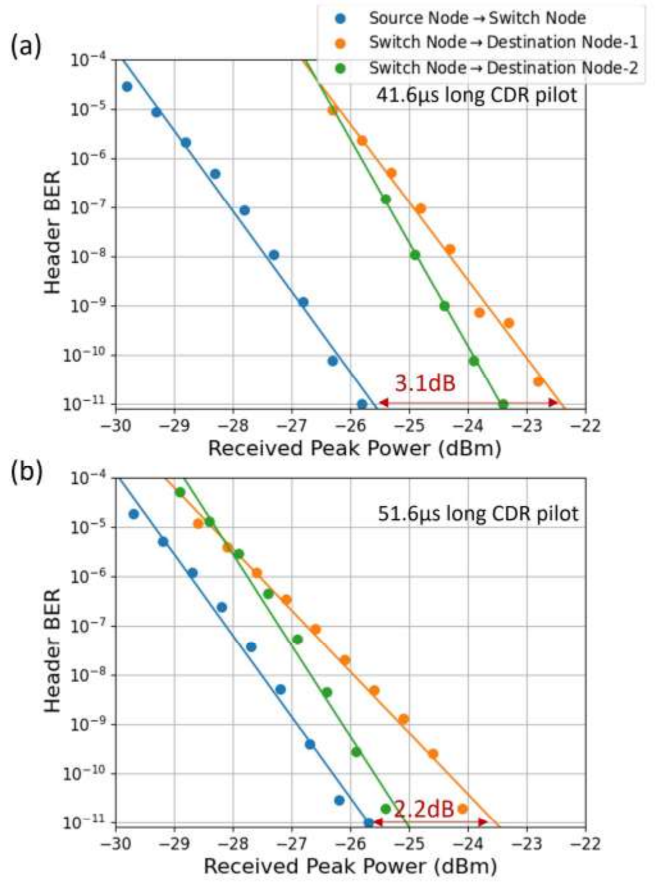

Fig. 9. Header BER measured at QWSR at the core (blue traces) and at the edges (orange and green trances) vs. received peak power for (a) 41.6 μs and (b) 51.6 μs long CDR pilot sequence.

to analyze the impact of the CDR pilot sequence length. There is 3.1 dB penalty between the destination nodes BER and the switch node. The penalty is due to the time difference between adjacent headers. As seen in the Fig. 2 A, B, and C, QWSR at the core lose the clock locking during only a single quantum payload time. In contrast, the edge nodes have more than two quantum payload duration gaps between the adjacent headers. Therefore, the clock synchronization loss is more severe for 41.6 μs long CDR pilot sequence. We increased the duration of the CDR pilot to 51.6 μs and observed that the BER penalty between the switch node and destination nodes decreased by 0.9 dB.

The processing and switching time of the QWSR depends on multiple factors such as optical switch speed, electronic circuits delay between the header detectors to the switch control port, FPGA's data processing time, etc. In the current implementation, the dominant factor is CDR circuit delay. QWSR can not receive the destination ID of the datagram before the CDR pilot sequence ends, which is 41.6 μs long. Therefore, either the QWSR should rely on the type of quantum memories (a versatile quantum device or fiber delay lines) to buffer the payload, or the datagram design should truncate the time assigned to the quantum payloads. However, there is no fundamental limitation to reducing the CDR pilot sequence to nanosecond ranges. Burst-mode CDR circuits are widely available; for example, Yu et al. [46] demonstrated a burst-mode CDR circuit with only 25 ns latency and no bit loss in the header for 10 Gbps data rate. When such a burst-mode CDR circuit is employed at the QWSR, quantum payloads can be buffered by a $\sim$5 meters of fiber with the expense of almost no loss. Another implementation might be synchronizing all QWSR at the cores and edges by a global optical clock distribution and phase caching between the nodes [47]. This way, CDR time can be reduced further to $<$ 1 ns, which is not going to be the dominant factor in the QWSR packet switching time.

V. CONCLUSION

Quantum Networks promises to scale up quantum applications and enhance the capabilities of quantum technologies. However, many innovations are needed to develop quantum networks to a useful level much less one on par with today's classical networks. The classical network's physical layer infrastructure and network stacks can inspire quantum networking designs. The 'packet switching' concept provides low transmission latency, high network utilization, and robust signaling to classical networks, eventually leading to the classical internet. When the quantum networks consider packet switching, the network architecture and enabling hardware require innovations. At this point, Quantum Wrapper Networking is proposed, and preliminary experimental results are conducted to realize 'quantum packets.' QWN relies on the classical header and tail bits, which wrap the quantum data payloads to form QW datagrams. QWN transports the datagrams end-to-end by routing the packets in the intermediate nodes without disturbing the fragile quantum data payloads; it further monitors and manages the network benefiting from copropagating classical header bits. In this work, we experimentally realize the packet switching in a three-node QWN testbed with 20 km fiber transmission link and achieve $>$20 CAR at both destinations and clear visibility, $>$79% for both HV and DA bases. We investigate the fiber channel impairments such as chromatic dispersion and polarization state rotations. Moreover, the correlations between the header BER and the payload CAR are reported for three separate network paths. The correlation results lead to performance monitoring in QWNs, like quality of transmission and could in the future be a tool for route optimization and traffic engineering. Although QW datagram designs can be flexible and support various network formats simultaneously, there are limitations in the header content and duration, especially the clock-data recovery pilot sequence. We employ DWDM commercial 10 Gbps SFPs as the QW header transceivers and analyze the CDR circuit limitations. While the current implementation suffers in terms of packet switching time and the header duration, we pave the way for future fast packet switching by improving CDR locking time. In the future, QWN can facilitate network control and management as capable as today's classical networks by utilizing the quantum wrapper datagrams.

REFERENCES

[1] C. Couteau et al., "Applications of single photons to quantum communication and computing," *Nature Rev. Phys.*, vol. 5, no. 6, pp. 326–338, 2023, [Online]. Available: https://www.nature.com/articles/s42254-023-00583-2

[2] D. Gottesman, T. Jennewein, and S. Croke, "Longer-baseline telescopes using quantum repeaters," *Phys. Rev. Lett.*, vol. 109, no. 7, 2012, Art. no. 070503, doi: 10.1103/PhysRevLett.109.070503.

[3] N. Gisin et al., "Quantum cryptography," *Rev. Modern Phys.*, vol. 74, no. 1, 2002, Art. no. 145, doi: 10.1103/RevModPhys.74.145.

[4] A. Aspuru-Guzik and P. Walther, "Photonic quantum simulators," *Nature Phys.*, vol. 8, no. 4, pp. 285–291, 2012. [Online]. Available: https://www.nature.com/articles/nphys2253

[5] C. Couteau et al., "Applications of single photons in quantum metrology, biology and the foundations of quantum physics," *Nature Rev. Phys.*, vol. 5, no. 6, pp. 354–363, 2023. [Online]. Available: https://www.nature.com/articles/s42254-023-00589-w

[6] T. R. Bromley et al., "Applications of near-term photonic quantum computers: Software and algorithms," *Quantum Sci. Technol.*, vol. 5, no. 3, 2020, Art. no. 034010, doi: 10.1088/2058-9565/ab8504.

[7] Z. Zhang and Q. Zhuang, "Distributed quantum sensing," *Quantum Sci. Technol.*, vol. 6, no. 4, 2021, Art. no. 043001, doi: 10.1088/2058-9565/abd4c3.

[8] D. Cuomo, M. Caleffi, and A. S. Cacciapuoti, "Towards a distributed quantum computing ecosystem," *IET Quantum Commun.*, vol. 1, no. 1, pp. 3–8, 2020, doi: 10.1049/iet-qtc.2020.0002, doi: 10.1049/iet-qtc.2020.0002.

[9] F. Arute et al., "Quantum supremacy using a programmable superconducting processor," *Nature*2019, vol. 574, no. 7779, pp. 505–510, 2019, https://www.nature.com/articles/s41586-019-1666-5

[10] J. M. Gambetta, J. M. Chow, and M. Steffen, "Building logical qubits in a superconducting quantum computing system," *npj Quantum Inf.*, vol. 3, no. 1, pp. 1–7, 2017, https://www.nature.com/articles/s41534-016-0004-0

[11] C. D. Bruzewicz et al., "Trapped-ion quantum computing: Progress and challenges," *Appl. Phys. Rev.*, vol. 6, no. 2, 2019, doi: 10.1063/2F1.5088164.

[12] M. Pompili et al., "Realization of a multinode quantum network of remote solid-state qubits," *Science*, vol. 372, no. 6539, pp. 259–264, 2021, doi: 10.1126/science.abg1919.

[13] T. M. Graham et al., "Multi-qubit entanglement and algorithms on a neutral-atom quantum computer," *Nature*, vol. 604, no. 7906, pp. 457–462, 2022, https://www.nature.com/articles/s41586-022-04603-6

[14] S. Lloyd et al., "Infrastructure for the quantum internet," *Comput. Commun. Rev.*, vol. 34, no. 5, pp. 9–20, 2004.

[15] W. K. Wootters and W. H. Zurek, "A single quantum cannot be cloned," *Nature*, vol. 299, no. 5886, pp. 802–803, 1982, https://www.nature.com/articles/299802a0

[16] Y. A. Chen et al., "An integrated space-to-ground quantum communication network over 4,600 kilometres," *Nature*, vol. 589, no. 7841, pp. 214–219, 2021, https://www.nature.com/articles/s41586-020-03093-8

[17] J. Chung et al., "Illinois express quantum network (IEQNET): Metropolitan-scale experimental quantum networking over deployed optical fiber," vol. 11726, Art. no. 1172602, 2021, doi: 10.1117/12.2588007, https://www.spiedigitallibrary.org/conference-proceedings-of-spie/1172

[18] S. K. Joshi et al., "A trusted node-free eight-user metropolitan quantum communication network," *Sci. Adv.*, vol. 6, no. 36, 2020, doi: 10.1126/sciadv.aba0959.

[19] C. H. Park et al., "2×N twin-field quantum key distribution network configuration based on polarization, wavelength, and time division multiplexing," *Npj Quantum Inf.*, vol. 8, no. 1, pp. 1–12, 2022, https://www.nature.com/articles/s41534-022-00558-8

[20] M. Pompili et al., "Experimental demonstration of entanglement delivery using a quantum network stack," *npj Quantum Inf.*, vol. 8, no. 1, pp. 1–10, 2022, https://www.nature.com/articles/s41534-022-00631-2

[21] R. Wang et al., "A dynamic multi-protocol entanglement distribution quantum network," in *Proc IEEE Opt. Fiber Commun. Conf. Exhib.*, 2022, pp. 1–3.

[22] S. Wengerowsky et al., "An entanglement-based wavelength-multiplexed quantum communication network," *Nature*, vol. 564, no. 7735, pp. 225–228, 2018.

[23] A. Dahlberg et al., "A link layer protocol for quantum networks," in *Proc. ACM Special Int. Group Data Commun.*, 2019, pp. 159–173, doi: 10.1145/3341302.3342070.

[24] O. Alia, R. S. Tessinari, E. Hugues-Salas, G. T. Kanellos, R. Nejabati, and D. Simeonidou, "Dynamic DV-QKD networking in trusted-node-free software-defined optical networks," *J. Lightw. Technol.*, vol. 40, no. 17, pp. 5816–5824, Sep. 2022, doi: 10.1109/JLT.2022.3183962.

[25] Y. Lee et al., "A quantum router architecture for high-fidelity entanglement flows in quantum networks," *npj Quantum Inf.*, vol. 8, no. 1, pp. 1–8, 2022, https://www.nature.com/articles/s41534-022-00582-8

[26] I. Lucio-Martinez et al., "Proof-of-concept of real-world quantum key distribution with quantum frames," *New J. Phys.*, vol. 11, no. 9, 2009, Art. no. 095001, doi: 10.1088/1367-2630/11/9/095001.

[27] S. DiAdamo et al., "Packet switching in quantum networks: A path to the quantum internet," *Phys. Rev. Res.*, vol. 4, 2022, Art. no. 043064, doi: 10.1103/PhysRevResearch.4.043064.

[28] S. J. Ben Yoo and P. Kumar, "Quantum wrapper networking," in *Proc. IEEE Photon. Conf.*, 2021, pp. 1–2.

[29] S. J. B. Yoo, "Optical packet and burst switching technologies for the future photonic internet," *J. Lightw. Technol.*, vol. 24, no. 12, pp. 4468–4492, Dec. 2006.

[30] S. J. B. Yoo et al., "Quantum wrapper networking," *IEEE Commun. Mag.*, doi: 10.1109/MCOM.001.2300067.

[31] S. K. Singh et al., "Experimental demonstration of correlation between copropagating quantum and classical bits for quantum wrapper networking," in *Proc. Eur. Conf. Opt. Commun.*, 2022, Art. no. Tu3B.3, https://opg.optica.org/abstract.cfm?URI=ECEOC-2022-Tu3B.3

[32] M. B. On et al., "Demonstration of quantum channel monitoring via quantum wrappers," in *Opt. Fiber Commun. Conf. Exhib.*, 2023, pp. 1–3.

[33] M. Mirhosseini et al., "Superconducting qubit to optical photon transduction," *Nature*, vol. 588, no. 7839, pp. 599–603, 2020, doi: 10.1038/s41586-020-3038-6.

[34] M. Forsch et al., "Microwave-to-optics conversion using a mechanical oscillator in its quantum ground state," *Nature Phys.*, vol. 16, no. 1, pp. 69–74, 2020, doi: 10.1038/s41567-019-0673-7.

[35] T. P. McKenna et al., "Cryogenic microwave-to-optical conversion using a triply resonant Lithium-Niobate-on-sapphire transducer," *Optica*, vol. 7, no. 12, pp. 1737–1745, 2020, https://opg.optica.org/optica/abstract.cfm?URI=optica-7-12-1737

[36] R. B. Jin et al., "Highly efficient entanglement swapping and teleportation at telecom wavelength," *Sci. Rep.*, vol. 5, no. 1, pp. 1–7, 2015, https://www.nature.com/articles/srep09333

[37] F. Samara et al., "Entanglement swapping between independent and asynchronous integrated photon-pair sources," *Quantum Sci. Technol.*, vol. 6, no. 4, 2021, Art. no. 045024, doi: 10.1088/2058-9565/abf599.

[38] E. Shchukin and P. Van Loock, "Optimal entanglement swapping in quantum repeaters," *Phys. Rev. Lett.*, vol. 128, no. 15, 2022, Art. no. 150502, doi: 10.1103/PhysRevLett.128.150502.

[39] Q.-C. Sun et al., "Entanglement swapping over 100 km optical fiber with independent entangled photon-pair sources," *Optica*, vol. 4, no. 10, pp. 1214–1218, 2017, https://opg.optica.org/optica/abstract.cfm?URI=optica-4-10-1214

[40] S. Muralidharan et al., "Optimal architectures for long distance quantum communication," *Sci. Rep.*, vol. 6, no. 1, Art. no. 20463, 2016, doi: 10.1038/srep20463.

[41] J. Yin et al., "Entanglement-based secure quantum cryptography over 1,120 kilometres," *Nature*, vol. 582, no. 7813, pp. 501–505, 2020, doi: 10.1038/s41586-020-2401-y.

[42] J. Wang et al., "Time-interleaved C-band Co-propagation of quantum and classical channels," 2023, *arXiv:2304.13828*.

[43] R. Mandil et al., "Quantum key distribution in a packet-switched network," *npj Quantum Inf.*, vol. 9, no. 1, Art. no. 85, 2023, doi: 10.1038/s41534-023-00757-x.

[44] C. Liang et al., "Characterization of fiber-generated entangled photon pairs with superconducting single-photon detectors," *Opt. Exp.*, vol. 15, no. 3, pp. 1322–1327, 2007, https://opg.optica.org/oe/abstract.cfm?URI=oe-15-3-1322

[45] J. Kelley, A. Forencich, G. C. Papen, and W. M. Mellette, "Characterization of burst-mode links for optical circuit switching," *J. Lightw. Technol.*, vol. 40, no. 9, pp. 2823–2829, May 2022.

[46] R. Yu, R. Proietti, S. Yin, J. Kurumida, and S. J. B. Yoo, "10-Gb/s BM-CDR circuit with synchronous data output for optical networks," *IEEE Photon. Technol. Lett.*, vol. 25, no. 5, pp. 508–511, Mar. 2013.

[47] K. A. Clark et al., "Synchronous subnanosecond clock and data recovery for optically switched data centres using clock phase caching," *Nature Electron.*, vol. 3, no. 7, pp. 426–433, 2020, https://www.nature.com/articles/s41928-020-0423-y

Mehmet Berkay On received the B.S. degree in electrical and electronics engineering from Bilkent University, Ankara, Turkey, in 2018. He is currently working toward the Ph.D degree in electrical and computer engineering with the University of California, Davis, CA, USA. His research interests include energy-efficient photonic neuromorphic computing, RF-photonic signal processing, fiber-optic communication/networking, and quantum networks.

Roberto Proietti received the M.S. degree in telecommunications engineering from the University of Pisa, Pisa, Italy, in 2004, and the Ph.D. degree in electrical engineering from Scuola Superiore Sant Anna, Pisa, in 2009. He was a Project Scientist with the University of California, Davis, CA, USA. He is currently an Assistant Professor with Politecnico di Torino, Turin, Italy. His research interests include optical switching technologies and architectures for super computing and data center applications, high spectral-efficiency coherent transmission systems, and elastic optical networking.

Gamze Gül (Graduate Student Member, IEEE) received the B.S. from Bilkent University, Ankara, Turkey, in 2017, and the M.S. from Koc University, Istanbul, Turkey, in 2019. She is currently working toward the Ph.D. degree with Northwestern University, Evanston, IL, USA. Her research interests include quantum communications and integrated photonics.

Gregory S. Kanter received the Masters of Engineering Management and Ph.D. degrees from Northwestern University, Evanston, IL, USA. He is currently a Research Professor with the Electrical and Computer Engineering Department, Northwestern University, and the Executive Director with NuCrypt, LLC, Park Ridge, IL, USA, where he has overseen the commercialization of a suite of instrumentation for use in quantum optics. His research interests include the generation and distribution of quantum states of light, optical communications, and radio-frequency photonics.

Sandeep Kumar Singh received the M.S. degree from Indian Institute of Technology Madras, Chennai, India, in 2014, and the Ph.D. degree from the Technical University of Braunschweig, Braunschweig, Germany, in 2019. He was a Research Scientist with German Aerospace Center, and a Postdoctoral Scholar with the University of California, Davis, CA, USA. He is currently an Assistant Professor with the Indian Institute of Technology, Roorkee, India. His research interests include quantum networking and data center networking.

Prem Kumar (Life Fellow, IEEE) is currently a Professor of information technology with the McCormick School of Engineering and Applied Science, Northwestern University, Evanston, IL, USA, primary appointment with the Department of Electrical and Computer Engineering. He has coauthored the National Academies report: *Optics and Photonics: Essential Technologies for Our Nation*, which spawned the National Photonics Initiative (NPI). He is also on the NPI Steering Committee, lending his expertise to issues pertaining to the National Quantum Initiative. His research interests include quantum communications and networking for interconnecting future quantum computing and sensing systems. Dr. Kumar has was a Program Manager with DARPA, where he managed a portfolio of programs in basic and applied sciences. He was the recipient of the Program Manager of the Year Award in 2015 and Secretary of Defense Medal for Outstanding Public Service in 2016, Quantum Communication Award from Tamagawa University in Tokyo, Japan, and the Walder Research Excellence Award from the Provost's office at Northwestern University. He is the Editor-in-Chief of *Optica*, the flagship high-impact journal of Optica (formerly OSA). He has been a Distinguished Lecturer for the IEEE Photonics Society, Hermann A. Haus Lecturer at MIT, . He is a Fellow of all the relevant professional societies: Optica (formerly OSA), APS, IoP (U.K.), AAAS, and SPIE.

S. J. Ben Yoo (Fellow, IEEE) received the B.S., M.S., and Ph.D. degrees from Stanford University, Stanford, CA, USA, in 1984, 1986, and 1991, respectively. In 1991, he conducted research on nonlinear optical processes in quantum wells, a four-wave-mixing study of relaxation mechanisms in dye molecules, and ultrafast diffusion-driven photodetectors with Stanford University. In 1999, he was the Senior Research Scientist with Bellcore, leading technical efforts in integrated photonics, optical networking, and systems integration. He led the MONET testbed experimentation efforts, and participated in ATD/MONET systems integration and a number of standardization activities. He is currently a Distinguished Professor with the University of California (UC Davis), Davis, CA, USA. His research interests include 2-D/3-D photonic integration for future computing, cognitive networks, communication, imaging, navigation systems, micro/nano systems integration, future Internet, next-generation Internet, reconfigurable multiwavelength optical networks (MONET), wavelength interchanging cross connects, wavelength converters, vertical-cavity lasers, and high-speed modulators. He was the recipient of the DARPA Award for Sustained Excellence in 1997, the Bellcore CEO Award in 1998, the Mid-Career Research Faculty Award from UC Davis in 2004, and the Senior Research Faculty Award from UC Davis in 2011. He is the Fellow of OSA and NIAC.